Journal of
Materials Chemistry B

Materials for biology and medicine

rsc.li/materials-b

ROYAL SOCIETY
OF CHEMISTRY
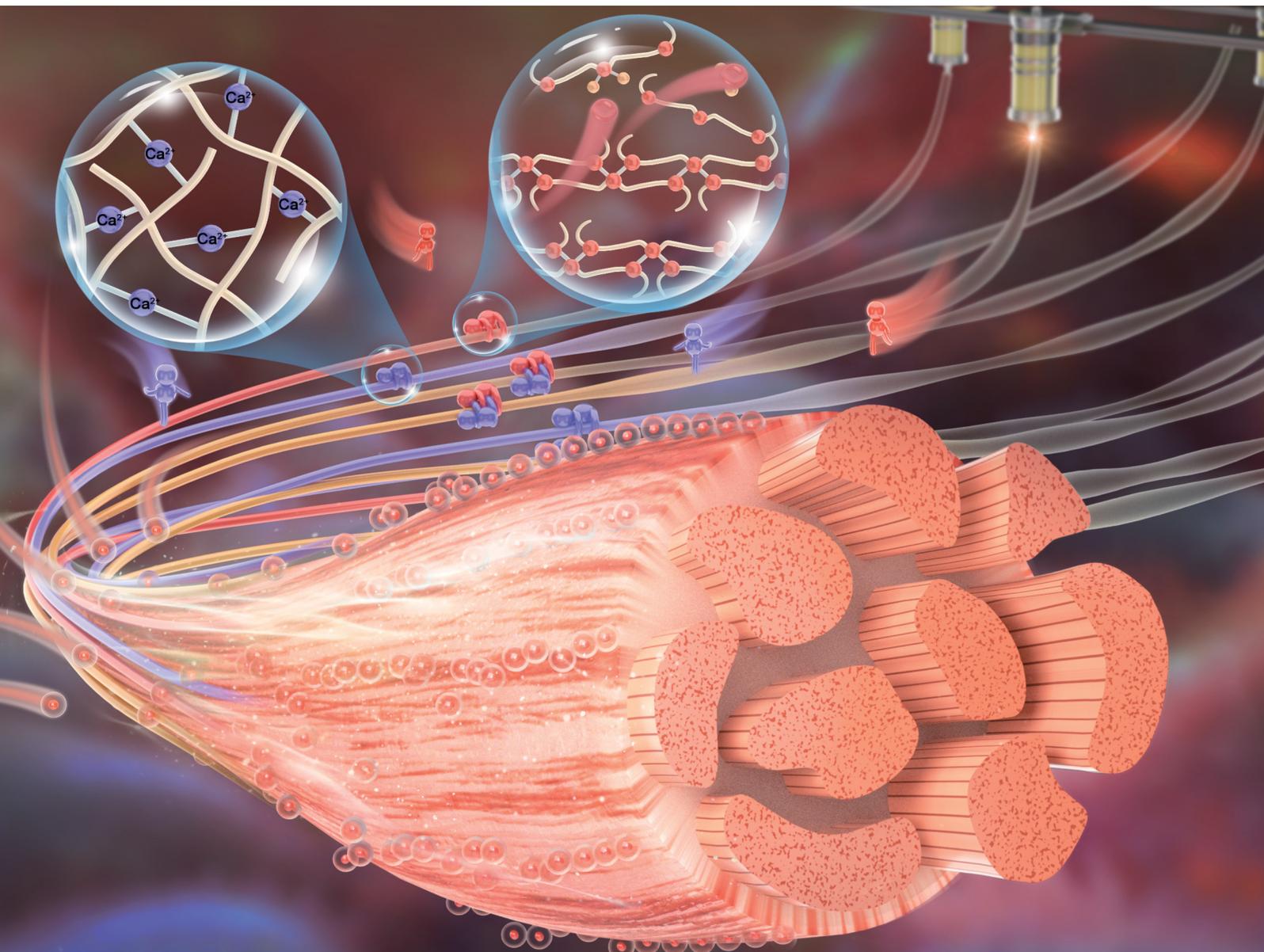
PAPER
Tao Jiang, Zirong Luo *et al.*
Fabrication and characterization of a multifunctional
alginate–gelatin–fibrinogen hydrogel for potential muscle
tissue reconfiguration *in vitro*

PAPER

Check for updates

Fabrication and characterization of a multifunctional alginate–gelatin–fibrinogen hydrogel for potential muscle tissue reconfiguration *in vitro*†

Zening Lin, [ID] Yang Hong, Tao Jiang, [ID] * Yun Yang, Yuan Gao, Hang Xie and Zirong Luo*

In recent years, Matrigel–fibrinogen–thrombin (MFT) hydrogels have gained prominence in muscle tissue regeneration and biohybrid robotics owing to their remarkable bioactivity. Nevertheless, addressing their disadvantages—the instability of Matrigel, inadequate mechanical strength, complex fabrication processes, and limited structural tunability of MFT hydrogels—while maintaining biocompatibility remains challenging. In this study, sodium alginate and gelatin are used to formulate an alginate–gelatin–fibrinogen hydrogel that avoids the operational complexity associated with the initial cross-linking of thrombin and the instability of Matrigel. Notably, the alginate–gelatin–fibrinogen hydrogel showed significant shear-thinning behavior and exhibited good printability for different structures. This approach overcomes the critical limitations of extrusion printing using MFT hydrogels to fabricate muscle tissue structures with different requirements. We also used a novel quality assessment method proposed in our previous study, which incorporates the relative mean width ($Rel.\bar{X}$) and relative standard deviation ($Rel.SD$) of extruded filaments to quantitatively evaluate printing quality. This approach enables the realization of an ideal printing boundary. In addition, a comparison with the Young's modulus of MFT hydrogels revealed that alginate–gelatin–fibrinogen hydrogels crosslinked with calcium chloride possessed significantly improved mechanical properties. The dual-crosslinking mechanism achieved *via* enzymatic and/or ionic methods resulted in flexible tunability of the modulus and porosity of the material. Experimental findings using C2C12 myoblast cells grown on the alginate–gelatin–fibrinogen hydrogel surface demonstrate that this biomaterial facilitates 3D bioprinting of anatomically complex muscle tissue constructs and biohybrid robotic systems. Overall, this study provides a novel strategy for the application in muscle tissue construction, repair, and bio-robotics through designing alginate–gelatin–fibrinogen composite hydrogels.

1. Introduction

Natural polymers are widely used in tissue engineering and regenerative medicine because of their high biological activity.[1,2] Matrigel, a material rich in laminin, type IV collagen, and other growth factors, is often used to construct *in vitro* tumor models for drug testing. For instance, Lee *et al.*[3] fabricated *in vitro* cancer models using Matrigel for differential gene expression research and drug screening. Fibrin is a natural hydrogel formed from fibrinogen *via* a series of reactions with

College of Intelligence Science and Technology, National University of Defense
Technology, Changsha, 410073, China. E-mail: jiangtao@nudt.edu.cn,
luozirong@nudt.edu.cn

thrombin. The amino acid sequences present in fibrin can promote cell adhesion, proliferation, and differentiation, making it a suitable scaffold material for applications such as vessel fabrication and tissue repair.[4,5] For example, Schöneberg *et al.*[6] used a collagen–fibrin hydrogel to create an *in vitro* vascular model with a wall thickness of 425 μm. This model could be dynamically cultivated in three weeks under physiological flow conditions.

Matrigel and fibrinogen are two highly bioactive materials currently used in tissue engineering and regenerative medicine. Nonetheless, scientists intend to broaden their use in fields such as microfluidic platforms and biohybrid robotics.[7] For example, Bashir *et al.*[8] combined Matrigel–fibrinogen–thrombin (MFT) hydrogel with C2C12 cells to create a wireless, light-responsive walking robot on a centimeter scale, which could accomplish walking, twisting, and other motions. Tao *et al.*[9]

used rat primary cardiomyocytes with MFT hydrogel to create a muscle actuator that lasted for at least six days, with the highest frequency of 5.6 Hz.

However, the MFT hydrogel currently used to make bio-hybrid robots has several disadvantages: (1) Inadequate mechanical properties. MFT hydrogels have low strength, and the structure can be easily damaged when transferred to the rack. Meanwhile, low stiffness can cause the structure to deform easily during movement and hence affect its movement performance. (2) The performance of the Matrigel is unstable. Different batches of Matrigel extracted from the interior of mouse tumors show inconsistency in the content of active substances, which will affect the stability of active muscle tissue culture and *in vitro* performance. (3) The MFT preparation process is complex. Multiple structures cannot be constructed simultaneously due to the rapid reactions of fibrinogen and thrombin. (4) It is impossible to fabricate complex models. MFT hydrogel materials can only be molded by mold casting and cannot be extruded or printed. This restricts the ability to realize intricate forms and features.

To address the problems mentioned above, this study proposes a method that employs sodium alginate–gelatin instead of Matrigel; the components are cross-linked using thrombin and calcium chloride after extrusion-based 3D printing. Gelatin exhibits sol–gel transition at ambient temperature, along with excellent thixotropic properties that benefit extrusion bioprinting. In addition, alginate is a naturally bioinert polysaccharide that can achieve matrix integrity through ionic crosslinking with divalent cations under physiological temperatures.[10] The chemical properties of alginate–gelatin are similar to the extracellular matrix (ECM).[11] These two materials can be used as rheology modifiers to promote the performance stability, mechanical properties, and printability of the MFT hydrogel,[12,13] thus clearing the roadblocks that limit its capability to fabricate complex 3D structures.

Here, alginate–gelatin–fibrinogen hydrogels were fabricated, and their morphological, porosity, rheological, swelling, degradation, and microscopic characteristics were characterized. A quantitative printing quality evaluation method proposed in our previous work was used to assess the printability of the bioink, and some demonstrative structures were printed for validation. The Young's moduli of the bioinks obtained with different crosslinking strategies and their biocompatibility were studied. This study serves as a foundational guide for overcoming the disadvantages of MFT hydrogels and paves the way for the performance improvement of future bio-robots. Meanwhile, it also provides a new method for muscle tissue regeneration and muscle damage repair in tissue engineering.

2. Materials and methods

The preparation and characterization of the alginate–gelatin–fibrinogen hydrogel (the molecular structures of the three materials are inspired by previous works[14,15]) are shown in Fig. 1.

2.1. Material preparation

Sodium alginate derived from brown algae was purchased from FMC Biopolymer (USA). Gelatin type B (from bovine skin), fibrinogen (from bovine serum), bovine serum albumin (BSA), aminocaproic acid (ACA), and thrombin (from bovine serum) were purchased from Sigma-Aldrich (USA). The enhanced cell counting kit-8 (ECCK-8) and calcein/PI cell viability/cytotoxicity assay kit (Calcein/PI assay) were purchased from Beyotime (Shanghai, China). Calcium chloride ($CaCl_2$) was obtained from Aladdin (Shanghai, China). C2C12 mouse myoblast cells and Dulbecco's modified Eagle medium (DMEM) were provided by Procell Life Science & Technology Co., Ltd (Wuhan, China). Fetal bovine serum (FBS) was obtained from Cellmax (China). Trypsin was purchased from Gibco (USA).

A 100 mM calcium chloride solution was prepared by adding 1.11 g of $CaCl_2$ particles to 100 mL of deionized water and shaken to dissolve. The BSA powder was added to deionized water to obtain a solution of 1 mg mL^{-1} concentration. The thrombin solution was prepared by dissolving the thrombin powder in the BSA solution to a final concentration thrombin of 20 units per mL. The ACA solution was prepared by dissolving the powder in distilled sterile water to make a stock solution of 50 mg mL^{-1}.[16] Then, 1 mL of ACA was added to 49 mL of GM (10% FBS) solution to make a supplemented growth medium (GM+).

Based on previous research,[17] alginate–gelatin bioinks (referred to as AxGy; x% alginate and y% gelatin) were prepared by dissolving sodium alginate and gelatin powders in DPBS and magnetically stirred at 60 °C for 1–2 h and then at 37 °C for 3 h until homogeneous. Then, the fibrinogen solution was prepared at a concentration of 8 mg mL^{-1} by dissolving it in DMEM. The alginate–gelatin–fibrinogen hydrogels with different material ratios were prepared by volumetrically mixing AxGy with the fibrinogen solution at a 1 : 1 ratio and stirring uniformly. The final concentrations were 0.5%, 1%, 1.5% for alginate, 7% for gelatin, and 0.4% for fibrinogen (referred to as A0.5G7F0.4, A1G7F0.4, A1.5G7F0.4). Finally, the hydrogels were centrifuged for 3 min to remove air bubbles.

2.2. Fourier transform infrared spectroscopy (FTIR) and scanning electron microscopy (SEM)

To confirm the presence of alginate, gelatin, and fibrinogen in the AxGyF0.4 composite hydrogels, FTIR spectroscopy was performed using a Thermo Scientific Nicolet iS20 equipped with an attenuated total reflectance (ATR). Samples of fibrinogen, AxG7, and AxG7F0.4 were freeze-dried before testing at room temperature.[18] The spectra were obtained from 4000 to 500 cm^{-1}.

To study the microscopic structures and morphology of the cross-linked hydrogels, AxG7F0.4 hydrogel samples were lyophilized using a freeze dryer (CREATRUST, China), metal-sprayed and characterized *via* SEM.[19]

2.3. Porosity calculation

The ethanol substitution method was used to quantify material porosity. The specific experimental process was as follows:[20]
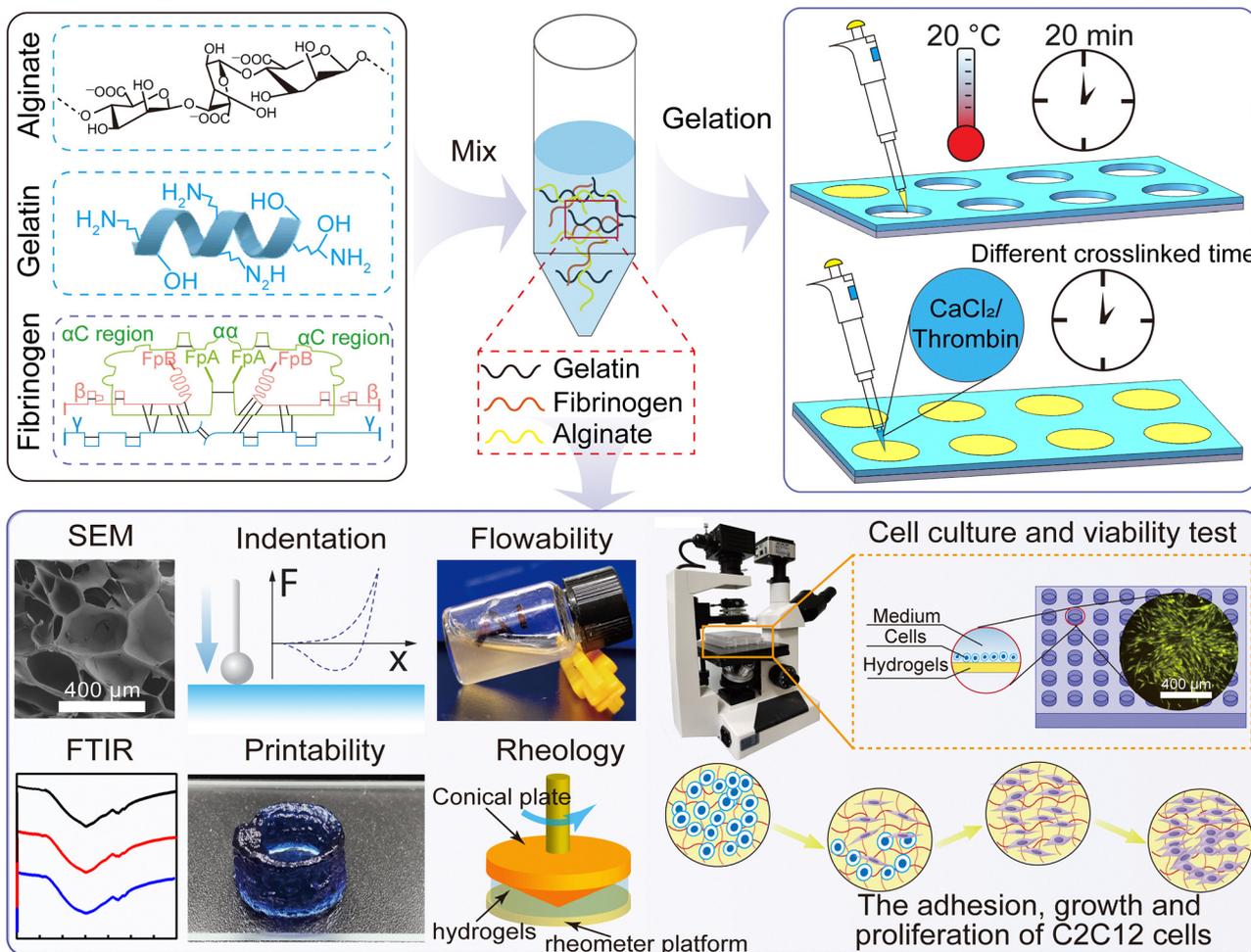
This journal is © The Royal Society of Chemistry 2025

J. Mater. Chem. B, 2025, **13**, 9824–9837 | **9825**

Fig. 1 Preparation and characterization methods for alginate−gelatin−fibrinogen composite hydrogels.

(1) the initial volume of ethanol was recorded as V_1; (2) the total volume (material + ethanol) was recorded as V_2; (3) after removal, the residual ethanol volume was recorded as V_3. Material porosity was then calculated as follows.

$$\frac{V_1 - V_3}{V_2 - V_3} \times 100\% \tag{1}$$

2.4. Flow state and rheological experiments

The flowability of the AxG7F0.4 hydrogels at different temperatures was assessed by inclining the gel containers and observing the flow behavior. The rheological properties of several AxG7F0.4 hydrogels and fibrinogen solutions were tested using a 20 mm cone plate geometry (with a cone apex angle of 1°) and a rheometer (HAAKE MARS III, ThermoScientific, USA). For all tests, the samples were placed on the surface of the platform. An extra solution squeezed out was removed using a scraper. A time sweep was performed at 20 °C to measure the responses of AxG7F0.4 hydrogels with different ratios and the fibrinogen solution as a function of time (20 min or 30 min). To obtain the gelling behavior of AxG7F0.4, a temperature sweep from 20 to 37 °C was performed at a constant frequency (1 Hz) and strain

amplitude (0.1%). Additionally, flow-curve sweeps were obtained at shear rates ranging from 0.1 s^{-1} to 100 s^{-1} at 20 °C. Meanwhile, stress sweep experiments were conducted by increasing oscillatory stress from 0.1 Pa to 3000 Pa at a constant frequency (1 Hz) and 20 °C. All tests were performed at least three times.

2.5. Extrusion tests of hydrogels and printability evaluation

Based on the principle of 3D extrusion bioprinting, we transformed a scrapped fused deposition modeling (FDM) printer in the laboratory into a simple 3D bioprinter for this study. In brief, the hydrogel was placed in 3cc cartridges and gelled at room temperature (20 °C) for 20 min. The microfilaments were printed by extrusion using G25 cylindrical nozzles (G25 Cyl, inner diameter = 0.26 mm) at a pressure of 100 kPa.

Based on our previous work,[21] different printing parameters, such as velocity and extrusion pressure, were varied in the printing setup to evaluate the printability of AxG7F0.4. A quantitative method described previously[21] was used to evaluate the quality of microfilaments. Specifically, 10 points were chosen to measure the width of a thin extruded line, and the average width $\bar{X}$ and standard deviation SD of these 10 points

were calculated.

$$\bar{X} = \frac{\sum x_i}{10}, \quad i = 1, 2, \ldots, 10 \tag{2}$$

$$SD = \sqrt{\frac{(x_i - \bar{X})^2}{9}}, \quad i = 1, 2, \ldots, 10 \tag{3}$$

Two dimensionless indices, namely relative mean width $Rel.\bar{X}$ and relative standard deviation $Rel.SD$, were defined as follows.

$$Rel.\bar{X} = \frac{\bar{X} - X_D}{X_D}, \quad Rel.SD = \frac{SD}{X_D} \tag{4}$$

A vector PA was introduced to cover both $Rel.\bar{X}$ and $Rel.SD$, and U is defined as the modulus of PA.

$$
\begin{aligned}
PA &= Rel.\bar{X}\boldsymbol{i} + Rel.SD\boldsymbol{j}, \\
U &= |PA| = \sqrt{(Rel.\bar{X})^2 + (Rel.SD)^2}
\end{aligned}
\tag{5}
$$

where X_D is the inner diameter of the nozzle. Under ideal conditions (when the filament is smooth and close to the theoretical width), $Rel.\bar{X}$ and $Rel.SD$ are both close to zero. $Rel.\bar{X}$ ranges from -1 to positive infinity; a positive value means that the extruded filament is wider than the designed filament and *vice versa*. $Rel.SD$ ranges from zero to positive infinity, with a higher value meaning the filament has greater smoothness.

2.6. Swelling and degradation tests

For the swelling experiments, after weighing the initial mass (W_d) of the samples, they were immersed in the culture medium and then moved to physiological conditions. The samples were weighed at intervals of t hours, and the mass of the samples was recorded as W_s. The swelling ratio was calculated as follows:[9]

$$S_r = \frac{W_s - W_d}{W_d} \times 100\% \tag{6}$$

The degradation rates under physiological conditions were quantified as described below: (1) the specimens were prepared for scheduled time points; (2) day 0 samples were lyophilized in liquid nitrogen, and their initial dry mass (W_d) was determined; (3) the remaining samples were maintained in physiological conditions (growth medium at 37 °C, pH 7.2–7.4); (4) the subsets were lyophilized every 4 days and their dry mass (W_t) was recorded. The equation of the degradation ratio is:

$$D_r = \frac{W_d - W_t}{W_d} \times 100\% \tag{7}$$

2.7. Micro-indentation test

The 3D models (diameter 35 mm and height 4 mm) were prepared using different cross-linking methods and crosslinking durations. After cross-linking, a micro-indenter was used to measure the stress–strain responses of the hydrogels at room temperature. The data were processed using the Hertz model

to obtain the corresponding Young's modulus. The Hertzian model was calculated as follows:[22]

$$F = \frac{4}{3} \times \frac{E}{1 - \mu^2} \times \sqrt{R}(\delta)^{\left(\frac{3}{2}\right)} \tag{8}$$

$$\delta = (x_2 - x_1) - \frac{F}{k} \tag{9}$$

where $(x_2 - x_1)$ is the translation movement distance of the load cell, and F/k denotes cell deformation. μ is the Poisson's ratio, R is the radius of the spherical sensor bead, and E is Young's modulus. Using $\delta^{\frac{3}{2}}$ and F as the new coordinates, the unloading phase indentation data was fitted to obtain the unloading phase slope k_2. The formula of Young's modulus was then derived as

$$E = \frac{F \cdot \frac{3}{4}(1 - \mu^2)}{(\delta)^{\frac{3}{2}} \cdot \sqrt{R}} = \frac{k_2 \cdot \frac{3}{4}(1 - \mu^2)}{\sqrt{R}} \tag{10}$$

2.8. Cell culture and cell viability assay

C2C12 mouse myoblasts were used to test cell viability in the AxGyF0.4 hydrogels and were cultured in a humidified incubator (37 °C with 5% CO_2). For C2C12 cells, DMEM mixed with 10% fetal bovine serum (FBS) and 1% penicillin–streptomycin antibiotics was used as the growth medium. In the cell culture, C2C12 mouse skeletal myoblasts were maintained until 60%–80% confluency to avoid differentiation. The cells were then seeded on the surface of the hydrogels after harvesting. Cell viability was measured by the ECCK-8 experiment and calcein/PI assay.[23]

2.9. Statistical analysis

All quantitative experimental data are presented as mean and standard deviation; analysis of variance (ANOVA) was used to verify statistical significance, and $p < 0.05$ was considered significant.

3. Results and discussion

3.1. The results of FTIR, SEM and porosity

Based on our previous work,[24] alginate–gelatin hydrogels reveal amide bands of gelatin, as well as polysaccharide and carboxylate bands for alginate. The same analytical method was used for the A1G7F0.4 hydrogel, and the result is shown in Fig. 2(a) and Table S1 (ESI†). The A1G7F0.4 hydrogel exhibited characteristic bands of the A1G7 hydrogel in the spectral range of 520–1630 cm^{-1}, indicating the successful incorporation of A1G7 components. Additionally, the characteristic bands of fibrinogen were also present, as well as a broad peak between 3000 and 4000 cm^{-1} for the O–H group of adsorbed water. The disappearance of several peaks in Fig. 2(a) suggests potential chemical bonds between fibrinogen and alginate–gelatin molecules. These bonds can be relatively weak such that the gel retains reversible flow behavior for a short time (Fig. S1, ESI†).
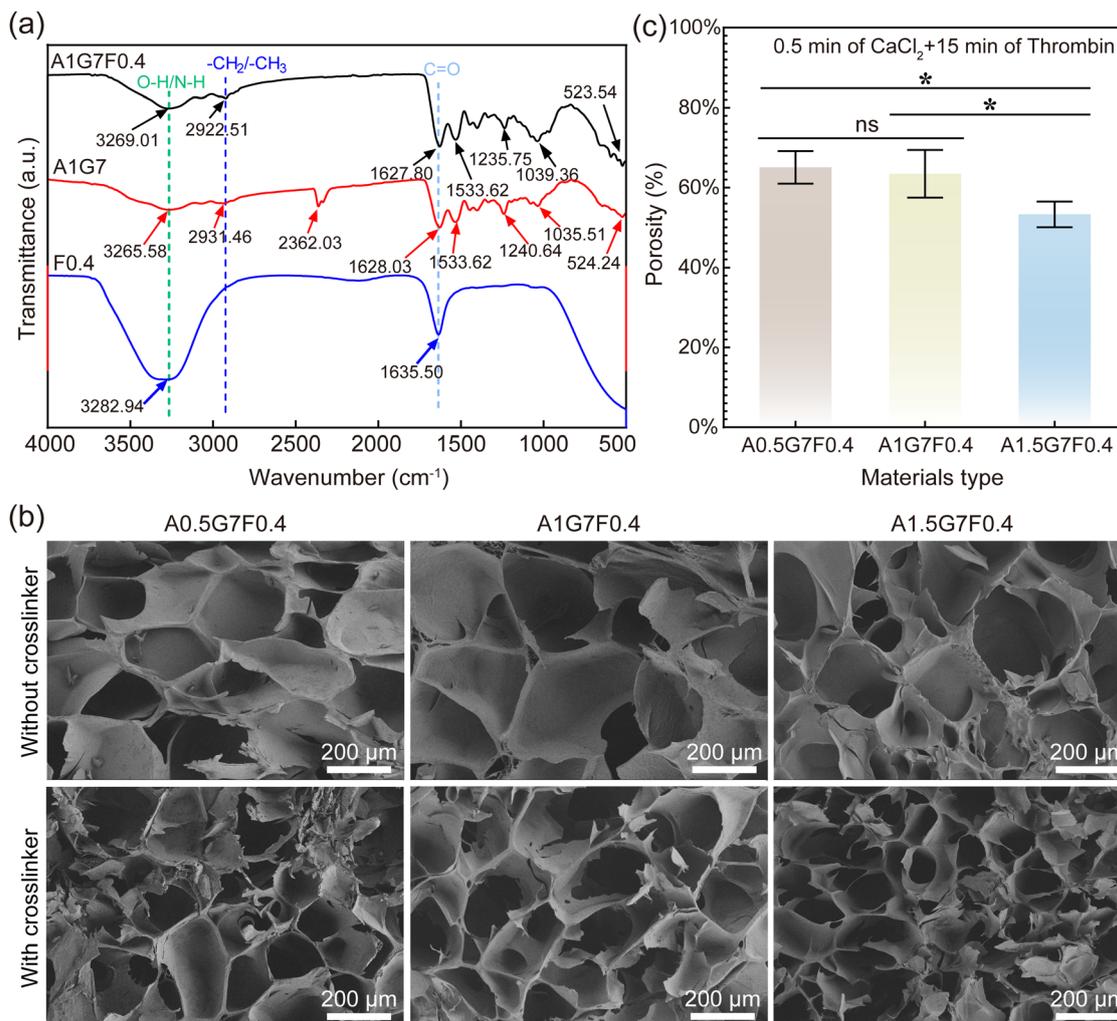
This journal is © The Royal Society of Chemistry 2025

J. Mater. Chem. B, 2025, **13**, 9824–9837 | **9827**

Fig. 2 The results of FTIR, SEM, and porosity tests. (a) FTIR results for A1G7F0.4, A1G7, and F0.4; (b) SEM images of AxG7F0.4 without and with the crosslinker, magnification = ×100; (c) Porosity of AxG7F0.4 after cross-linking.

The SEM analysis of AxG7F0.4 was then conducted to investigate the morphological characteristics, and the results are shown in Fig. 2(b) and Fig. S2 (ESI†). All samples displayed internal porous structures characterized by various pore sizes. A1G7F0.4 (144.32 ± 11.51 μm) and A1.5G7F0.4 (94.21 ± 10.38 μm) exhibited smaller pore sizes than A0.5G7F0.4 (170.99 ± 39.55 μm) after 20 min of gelation at room temperature. This reduction stems from the enhanced physical network density with increasing alginate concentrations. After crosslinking (0.5 min CaCl$_2$ + 15 min thrombin), the pore diameter further decreased to 141.86 ± 12.27 μm (A0.5G7F0.4), 140.79 ± 20.90 μm (A1G7F0.4), and 77.18 ± 12.33 μm (A1.5G7F0.4).

Porosity measurements revealed an inverse correlation between alginate concentration and porosity after crosslinking: A0.5G7F0.4 (65.07% ± 4.08%), A1G7F0.4 (63.44% ± 5.98%), and A1.5G7F0.4 (53.27% ± 3.22%) (Fig. 2(c)). Increasing alginate from 0.5% to 1.5% w/v significantly reduced pore size and porosity, which can be attributed to Ca^{2+} crosslinking. These porous architectures are favorable for nutrient storage and transportation, and the rough surface (Fig. S2, ESI†) can

provide a conducive environment for cell proliferation and adhesion. Different pore sizes may influence the mechanical properties and biocompatibility.

3.2. Rheological properties of the hydrogels

The rheological properties of hydrogels are key to their 3D printing performance, and the results are shown in Fig. 3 and Fig. S3–S6 (ESI†). G', G'' and η (or $|\eta^*|$) indicates the storage modulus, loss modulus, and viscosity, respectively. The AxG7F0.4 hydrogels had comparable solid and liquid characteristics (G' and G'' in the same magnitude) at the start of the test, as demonstrated in Fig. 3(a) and Fig. S4(a) (ESI†). Over time, the solid-like property strengthened rapidly, and G' increased faster than did G'', suggesting the formation of a cross-linked gel network with enhanced elastic properties. After a 30-minute gelation period, the storage moduli (G') of the MFT, A0.5G7F0.4, A1G7F0.4, and A1.5G7F0.4 hydrogels were measured as 140 kPa, 791 kPa, 1064 kPa, and 1129 kPa, respectively. The data demonstrate that the storage and loss modulus of the MFT hydrogel (at a concentration of fibrinogen
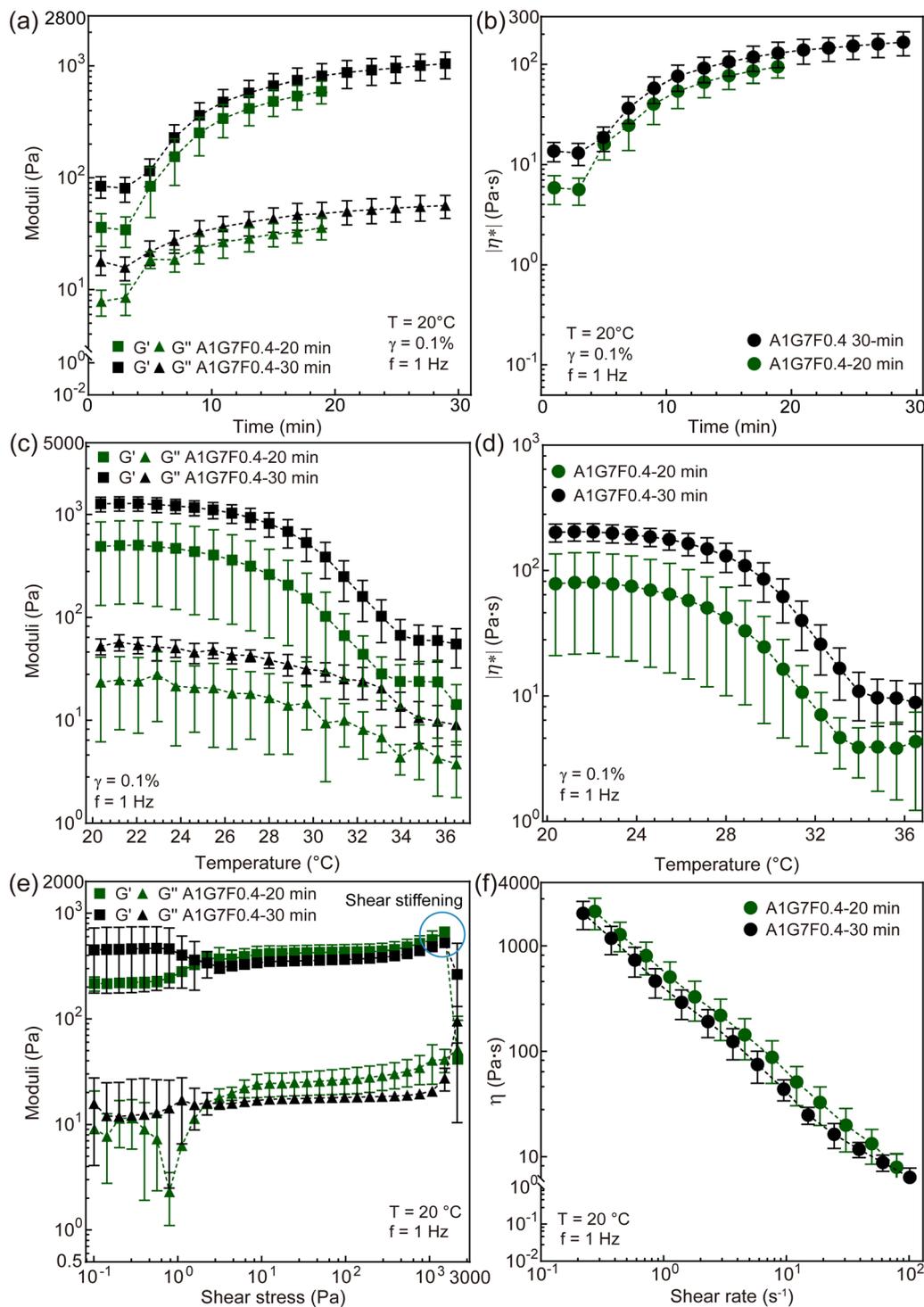
Fig. 3 Rheological properties of A1G7F0.4 and F0.4. (a) Storage (G') and loss moduli (G'') *versus* gelation time. (b) Complex viscosity *versus* gelation time. (c) G' and G'' *versus* temperature. (d) The variation of complex viscosity with respect to temperature from 20 to 37 °C. (e) G' and G'' *versus* shear stress. (f) Dynamic viscosity in the shear rate range of 0.1–100 s^{-1}.

4 mg mL^{-1}) considerably increased with the addition of alginate–gelatin, with alginate contributing to G'' and gelatin contributing to G', which was further supported by the loss tangent plots of AxG7F0.4 after 20 and 30 min of gelation (Fig. S3 and S5, respectively, ESI†). The rise in G' of the

AxG7F0.4 hydrogels gradually slowed down after 20 minutes of gelation, and the gel exhibited strong solid-like properties.

These results indicate that G' and G'' of the AxG7F0.4 hydrogels increase with the augmentation of alginate, with no significant differences observed for different alginate concentrations.

This journal is © The Royal Society of Chemistry 2025

J. Mater. Chem. B, 2025, **13**, 9824–9837 | **9829**

Based on our previous research,[10] it can be concluded that gelatin is the primary factor affecting the storage modulus. Notably, the A1.5G7F0.4 hydrogel exhibited a faster increase in viscosity over time and eventually reached a higher viscosity compared with the A0.5G7F0.4 hydrogel at 30 min (Fig. 3(b) and Fig. S4(b), ESI†), suggesting a more rapid gelation process and a tighter gel structure.

The temperature sweep analysis presented changes in the rheological characteristics of the AxG7F0.4 hydrogel in the range of 20–37 °C. G' and G'' of the AxG7F0.4 hydrogel dropped as the temperature increased (Fig. 3(c) and Fig. S4(c), ESI†), suggesting a transition from elastic-dominant to viscous-dominant behavior at higher temperatures. Specifically, the storage modulus decreased faster above ~25 °C and then levelled off. As the temperature increased, the viscosity dropped significantly before leveling out (Fig. 3(d) and Fig. S4(d), ESI†). This phenomenon indicates that the high sensitivity of the AxG7F0.4 viscosity to temperature is primarily attributed to the sol–gel transition of gelatin. Since insufficient G', G'', and viscosity can compromise the integrity of printed structures, the temperature of the printing experiment was controlled below 25 °C. Increasing the content of sodium alginate and fibrinogen can help increase the temperature adaptation window if lower temperature sensitivity is required.

The stress sweep analysis was subsequently conducted, and the results are shown in Fig. 3(e) and Fig. S6(a), (b) (ESI†). When stress increased to a certain threshold point, the hydrogel yielded and the storage modulus dropped abruptly, exhibiting a liquid-like state. At the yielding point, the loss modulus exhibited a sharp rise, presumably owing to the destruction and reorganization of the cross-linked network by the applied stress, leading to a sudden increase in energy dissipation. Besides, the yield stress values of A1G7F0.4 were about 1722 ± 163 Pa (gelling 20 min) and 1865 ± 193 Pa (gelling 30 min).

A flow-curve sweep was carried out to examine the shear-thinning behavior of the material. The non-zero intersection with the y-axis in Fig. S6(c) (ESI†), along with the results shown in Fig. 3(e), suggests the presence of yield stress for AxG7F0.4, which benefits the extrudability and structural integrity of the material during and post-printing. Meanwhile, the addition of alginate and gelatin to the hydrogel facilitates substantial shear thinning behavior, as shown in Fig. 3(f) and Fig. S6(d) (ESI†). When the ratio of the three components changed, the shear thinning behavior also changed accordingly.

Overall, the rheological results indicate that the addition of alginate and gelatin can considerably modify the rheological properties of the hydrogel, providing yield stress and strong shear-thinning behavior to the material, which are crucial for extrusion printing.

3.3. Printability evaluation

A temperature crosslinking time of 20 min was selected based on the above experimental results, and the remaining specific parameters were set as shown in Table 1. Tests were performed using the printing quality evaluation method proposed in Section 2.4, and statistical analyses of the microfilament printing results are shown in Fig. 4, 5 and Fig. S7, S8 (ESI†).

Table 1 The printing parameters set for AxG7F0.4

	Influencing factors	Parameter setting
Printing setup	Materials type	AxG7F0.4, x = 0.5, 1, 1.5
	Nozzles geometry	G25 tap (0.26 mm)
	Pneumatic pressure	55 kPa, 60 kPa, 65 kPa
	Translational velocity	6–18 mm s^{-1}, at intervals of 3 mm s^{-1}
	Gelling time	20 min
	Tip-to-platform separation	0.2 mm

The results show that the relative mean width ($Rel.\bar{X}$) has a strong negative correlation with translational velocity (Fig. 4(a) and Fig. S7(a)–(c), ESI†). Specifically, the $Rel.\bar{X}$ of A1G7F0.4 decreased from about 3.46 to 0.73 with an increase in translational speed from 6 to 18 mm s^{-1} under 55 kPa pressure (Fig. 4(a)). The $Rel.\bar{X}$ of the AxG7F0.4 hydrogel showed a positive correlation with pressure (Fig. 4(b)), while $Rel.SD$ exhibited an insignificant correlation with translational speed and pressure (Fig. 4(c) and (d)). The $Rel.SD$ values were more concentrated in the low-pressure regime regardless of translational speed, whereas they were more dispersed in the high-pressure regime (Fig. 4(d)). Besides, the developed hydrogels had higher $Rel.SD$ compared with pastes (e.g., Pluronic® F127) under similar printing conditions.[25] This can presumably be attributed to the relatively weak intermolecular interactions of pastes, allowing higher molecular mobility relative to each other.

To further investigate the effects of pressure and speed on printing accuracy, the coupled data were evaluated, and the results are shown in Fig. 5(a) and Fig. S8(a), (b) (ESI†). U and $Rel.\bar{X}$ decreased with decreasing ratios of pressure to velocity (P/V), while $Rel.SD$ did not exhibit an apparent correlation with P/V. Maintaining the pressure at a low level for stable extrusion can both result in better printing quality and alleviate shear damage to the cells incorporated in the gel.

As for printability values, the ideal printing window is $Rel.\bar{X} = 0$ and $Rel.SD = 0$ ($U = 0$). A majority of $Rel.\bar{X}$ values were between 1 and 6, and the $Rel.SD$ values were between 0.1 and 0.25 (Fig. S8(c), ESI†). In particular, $Rel.\bar{X}$ between 0 and 4 and $Rel.SD$ below 0.2 can be used as acceptable printing boundaries, while $Rel.\bar{X}$ between 0 and 2, and $Rel.SD$ below 0.15 are considered a relatively ideal printing quality regime (Fig. 5(b) and Fig. S8(c), ESI†). Upon comparing the changes in $Rel.\bar{X}$ and $Rel.SD$ values, it was evident that U is primarily influenced by $Rel.\bar{X}$ owing to its higher value than $Rel.SD$ (Fig. S8(d), ESI†). To simplify the data comparison process, other studies in this field initially employ U to determine the acceptable printing boundaries and subsequently seek the optimal printing domain based on actual requirements.

Several 3D structures (Fig. 5(c)) were printed, demonstrating the printability of the AxG7F0.4 hydrogels and their capability to print complex bionic geometries that simulate the functions of biological tissues. Meanwhile, the AxG7F0.4 hydrogels overcome the extrusion limitation inherent to MFT hydrogels by employing thermosensitive crosslinking.

3.4. Analysis of swelling and degradation characteristics

Solubility and degradation are the main factors that affect the mechanical properties of materials. All AxG7F0.4 hydrogels
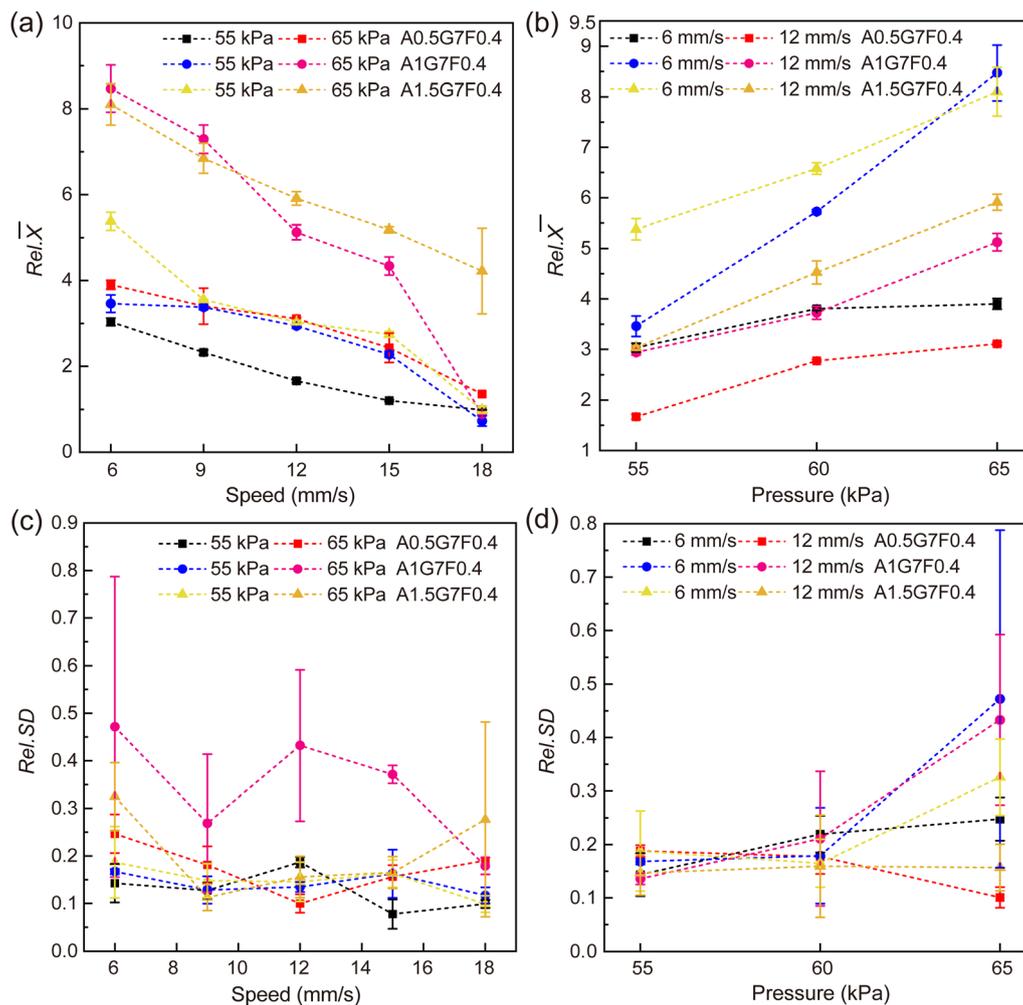
Fig. 4 Printability evaluation results for AxG7F0.4. Variations in $Rel.\bar{X}$ with (a) translational velocity and (b) extrusion pressure; $Rel.SD$ variations with (c) translational velocities and (d) extrusion pressure.

were gelled at 20 °C for 20 minutes, followed by crosslinking *via* CaCl₂ for 0.5 min and thrombin for an additional 15 min; the results are shown in Fig. 6. The experimental results show that A0.5G7F0.4 had a higher swelling ratio initially, and it gradually decreased after 12 hours of swelling (Fig. 6(a)). This phenomenon likely arises from elevated porosity, which facilitates accelerated water infiltration into the material. Then, the degradation rate exceeds the water absorption rate due to the sparse 3D network. The swelling ratio decreases as the sodium alginate concentration rises because more carboxyl groups join calcium ions to create calcium bridges, which compacts the network structure and promotes stiffness. Interestingly, A1.5G7F0.4 exhibited a higher swelling ratio than A1G7F0.4, showing a significant difference in the swelling equilibrium (Fig. 6(b)). This discrepancy may stem from the high viscosity of A3G14 before mixing FN, which either impedes the uniform formation of the 3D network or introduces localized micro-defects. Consequently, the interpenetrating network formed through double crosslinking demonstrated inferior synergy compared to A1G7F0.4. Notably, A1G7F0.4 exhibited a lower

equilibrium swelling ratio (11.11% ± 0.96%) than the fully crosslinked MFT hydrogel (12.5% ± 0.3%).[9] Furthermore, prolonged crosslinking duration led to a further reduction in the swelling ratio.

The degradation rate of AxG7F0.4 exhibited an inverse correlation with both alginate concentration and degradation duration. This phenomenon occurs because lower sodium alginate concentrations produce calcium alginate networks that are more susceptible to ion exchange or enzymatic disruption. On day 16, the degradation rates reached 68.84% ± 4.40%, 58.10% ± 4.53%, and 55.14% ± 3.49%, respectively for the tested formulations. While these results confirm the stable *in vivo* degradation capability of the materials, further optimization through prolonged crosslinking treatment can enhance degradation control.

3.5. Analysis of mechanical properties and the synergistic crosslinking mechanism

To study the effects of different cross-linking methods on the mechanical properties of the AxG7F0.4 hydrogels, a micro-indenter
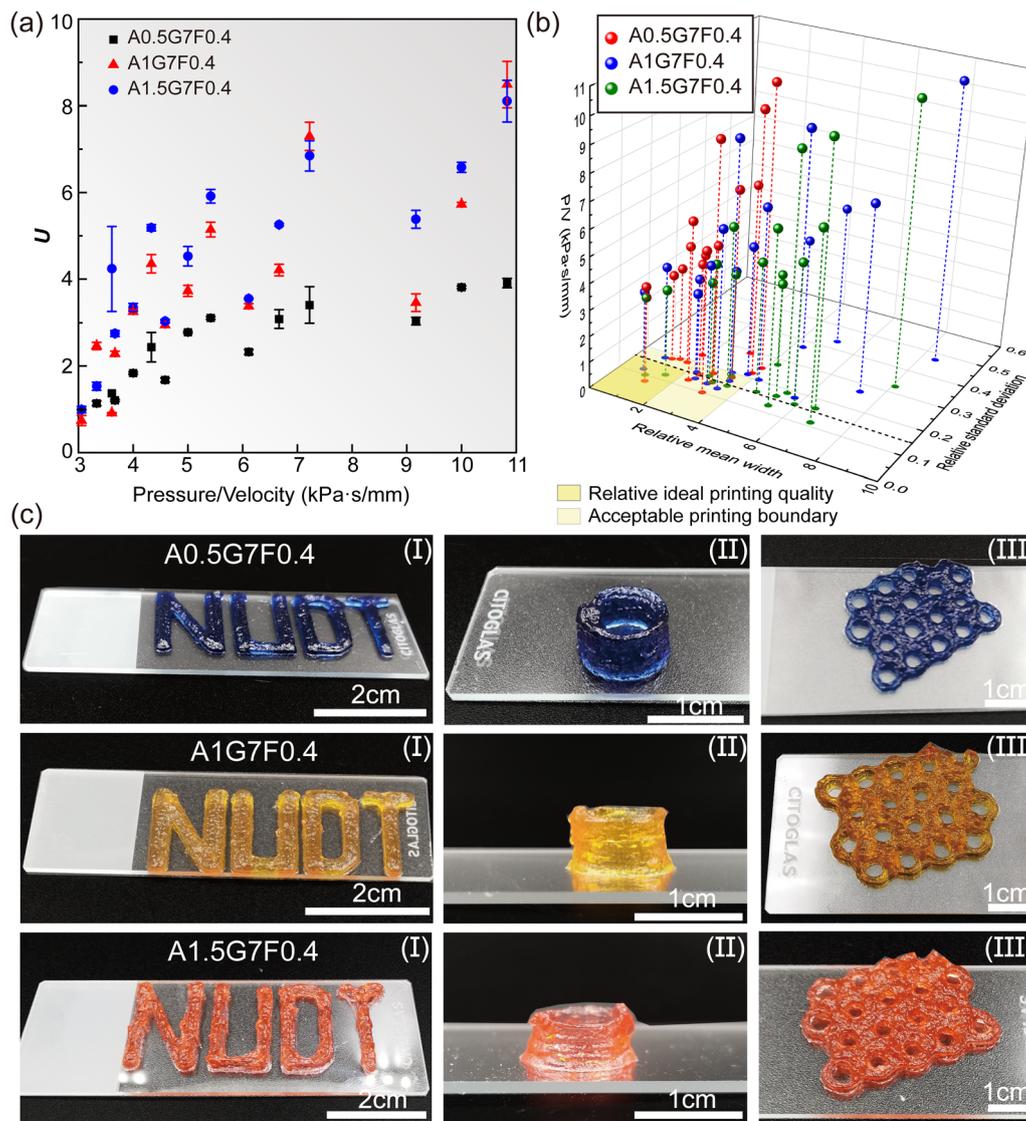
This journal is © The Royal Society of Chemistry 2025

J. Mater. Chem. B, 2025, **13**, 9824–9837 | **9831**

Fig. 5 U, $Rel.\bar{X}$, and $Rel.SD$ of different hydrogels under various pressure/velocity (P/V) values and 3D printed structures. (a) Variations in U with P/V. (b) $Rel.\bar{X}$ and $Rel.SD$ of AxG7F0.4 with relatively ideal printing zones, acceptable printable boundary has been colored. (c) Printed structures of AxG7F04: (I) printed thin-walled structure (the text ''NUDT''); (II) hollow cylinder (height 6 mm); (III) honeycomb structure.

was used to test the force-displacement responses. The different crosslinking conditions tested are shown in Table 2 and Table S2 (ESI†), and the results are shown in Fig. 7. The concentrations of $CaCl_2$ and thrombin were maintained at 100 mM and 20 units per mL, respectively.

The materials were first crosslinked at 20 °C for 20 minutes and then fully crosslinked using different crosslinking agents and durations.

The elastic moduli of hydrogel materials with three different ratios were compared after crosslinking with calcium chloride for different durations (Fig. 7(a)). Young's modulus increased by 154.69% when the concentration of sodium alginate was increased from 0.5% w/v to 1.5% w/v at a constant 0.5 min crosslinking time, showing a significant difference. A similar trend was also observed for 1 min crosslinking time. This indicates that even a small change in sodium alginate can have

a significant effect on the strength of the AxG7F0.4 hydrogels. This also confirms the above SEM and porosity results, indicating a negative correlation between modulus and pore size.

Compared with Young's modulus of the fully crosslinked MFT hydrogel (1.9 kPa),[9] the value of A1G7F0.4 cross-linked with calcium chloride for 1 minute was higher by 76% (Fig. 7(b)), and this result verifies the feasibility of the strategy. Further analysis revealed that the addition of either thrombin or $CaCl_2$ solution improved the Young's modulus of the hydrogel in comparison with the control group (group 1) (Fig. 7(b)). The A1G7F0.4 gel crosslinked using thrombin for 30 min and $CaCl_2$ solution for 0.5 min showed 32.35% and 36.06% higher elastic moduli, respectively, with no significant differences between the two. There was a noticeable distinction between groups 1 and 4, indicating the significant contribution of $CaCl_2$ crosslinking to Young's modulus. Generally, thrombin has a
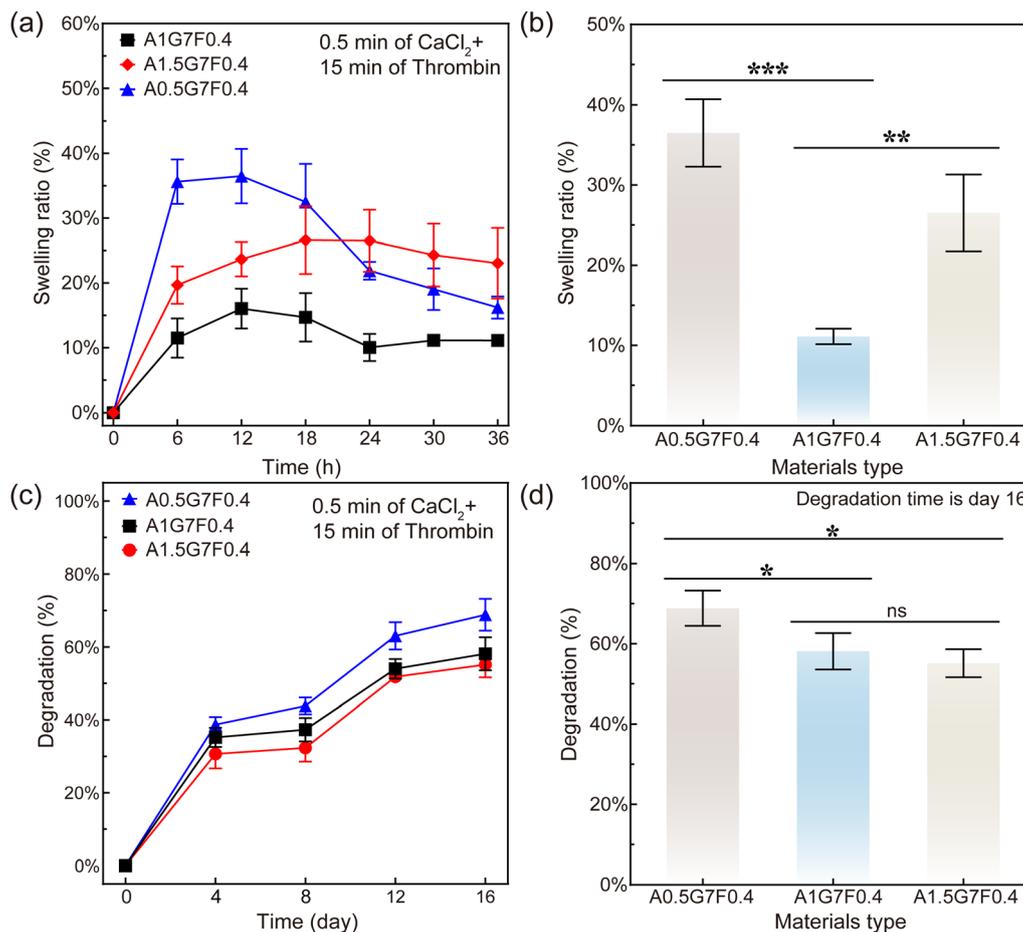
Paper

Fig. 6 The swelling and degradation characteristics of AxG7F0.4. (a) Variation in the swelling rate with time. (b) Significance analysis of the swelling rates of AxG7F0.4 hydrogels. (c) Variation in the degradation ratio with time. (d) Significance analysis of the degradation rate.

Table 2 The crosslinking conditions for the A1G7F0.4 hydrogels

Group	Material	Gelling temperature (°C)	Gelling time (min)	Crosslinking agent	Crosslinking time (min)
1	A1G7F0.4 hydrogels	20	20	—	—
2				Thrombin	30
3				CaCl$_2$	0.5
4					1
5				CaCl$_2$ + thrombin	0.5 + 15
6					0.5 + 30
7					1 + 15
8					1 + 30

much weaker crosslinking effect compared with CaCl$_2$, presumably due to the nature of the enzymatic crosslinking mechanism.[26] The addition of thrombin after crosslinking with CaCl$_2$ had an insignificant effect on Young's modulus, which can be attributed to the blockage of particle penetration because of the intertwined network generated by CaCl$_2$ crosslinking.

To elucidate the synergistic effects of dual crosslinking, we carried out comparative FTIR, SEM, and porosity and swelling analyses under three crosslinking conditions, including

CaCl$_2$ only, thrombin only, and combined CaCl$_2$/thrombin; the results are presented in Fig. 8. The FTIR spectra revealed no significant alterations in chemical bonding patterns across the three conditions, implying that the synergy arises from physical interactions or structural rearrangements rather than chemical modifications. Further examination of the peak intensities and full width at half maximum (FWHM) values in the 1650–1550 cm^{-1} range demonstrated intermediate characteristics of the dual-crosslinked samples compared with the single-crosslinked controls (Fig. 8(a)). Porosity measurements yielded values of 62.05% ± 5.05%, 62.99% ± 6.85%, and 49.79% ± 4.79% for CaCl$_2$-only, thrombin-only, and dual-crosslinked hydrogels, respectively, further validating the physical enhancement hypothesis. Prolonged swelling tests (36 h) revealed distinct performance profiles. The CaCl$_2$-only hydrogels exhibited high initial swelling ratios but demonstrated progressive structural degradation as sparse ionic crosslinks succumbed to solvent penetration. As for AxG7F0.4, the thrombin-only formulation showed rapid disintegration under physiological conditions due to insufficient network stabilization. This phenomenon could be attributed to low fibrinogen concentration. In contrast, the dual-crosslinked system maintained dimensional stability with a significantly lower
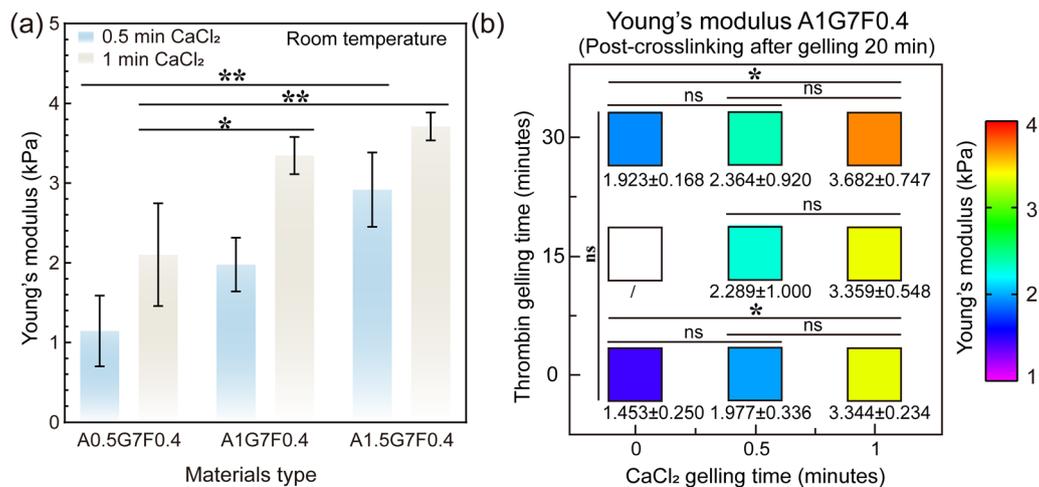
Fig. 7 The elastic modulus of the AxG7F0.4 hydrogels. (a) Comparison of the Young's moduli of AxG7F0.4 hydrogels; (b) Young's modulus of A1G7F0.4 prepared under different crosslinking conditions. **$p < 0.01$ and *$p < 0.05$.
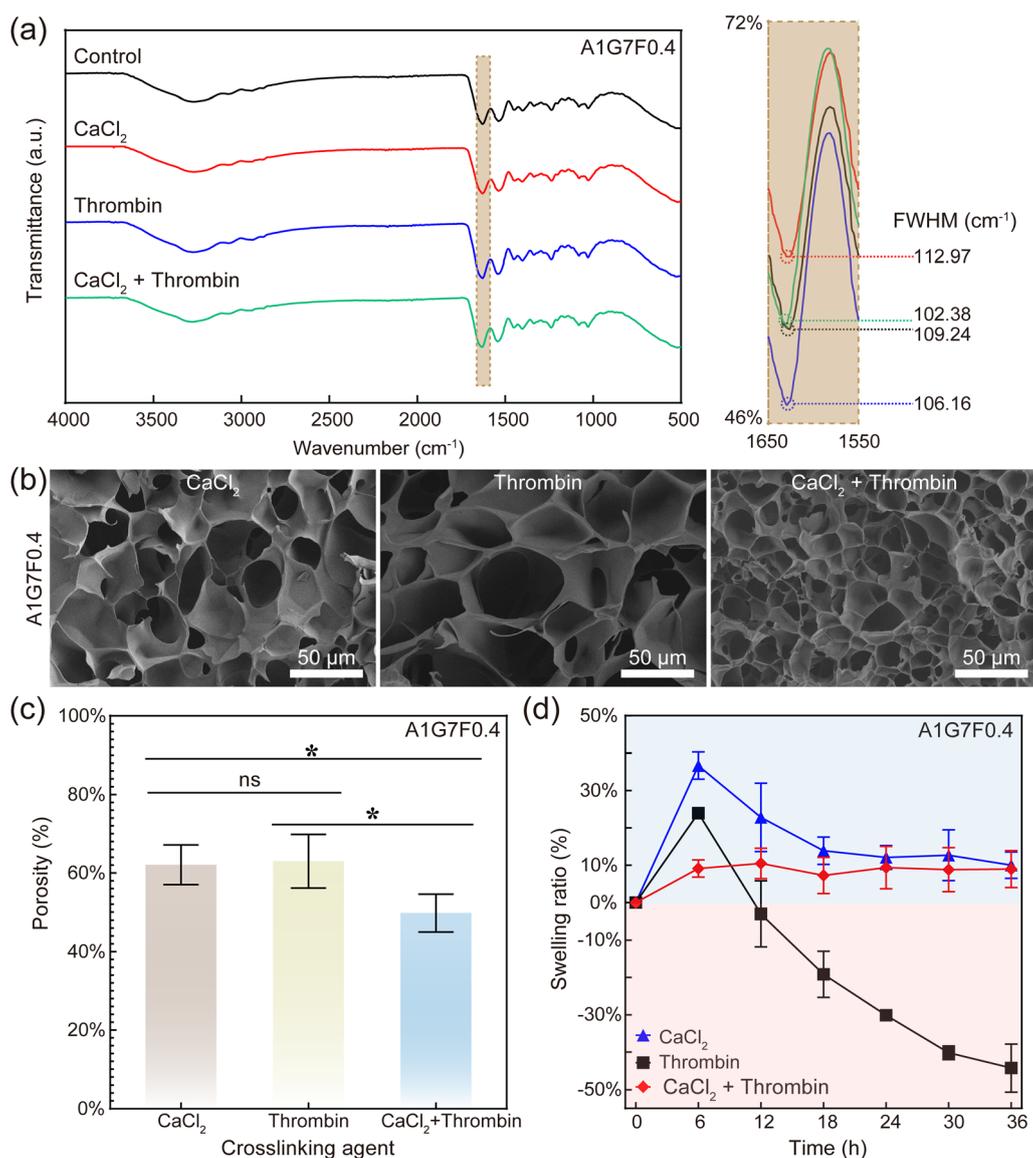

Fig. 8 Characterization of the synergistic crosslinking mechanism of $CaCl_2$ and thrombin. (a) FTIR results of different crosslinking agents used for A1G7F0.4; (b) SEM. Magnification = ×500; (c) A1G7F0.4 porosity under different crosslinking conditions; (d) variation in the swelling rate with time.

9834 | J. Mater. Chem. B, 2025, 13, 9824–9837

This journal is © The Royal Society of Chemistry 2025

equilibrium swelling ratio (8.81%) and sustained structural integrity. This behavior stems from the as-formed interpenetrating network: (1) rapid ionic crosslinking establishes a primary calcium–alginate scaffold, followed by (2) enzymatic fibrin polymerization that reinforces the matrix through covalent fibrinogen–thrombin interactions. This is due to the binding of sodium alginate with calcium ions to form calcium bridges, and this ionic crosslinking can quickly form a primary cross-linked network. Thrombin binds to fibrinogen to form fibrin, further stabilizing the structural integrity and increasing the cross-linking density, thereby forming an interpenetrating network.[26–28]

Notably, increased crosslinking time and sodium alginate concentration can affect cellular activity, and hence the crosslinking method needs to be tailored depending on the actual application.

3.6. Biocompatibility of the AxG7F0.4 hydrogels

Sterile AxG7F0.4 hydrogels were placed in 24-well plates and gelled at 20 °C for 20 minutes, followed by crosslinking using $CaCl_2$ for 0.5 min and thrombin for an additional 15 min. C2C12 cells are seeded on the gel at a density of 2×10^4 cells per well. The calcein/PI assay was used to test cell viability after culturing for 1, 3, and 5 days, and the results are shown in Fig. 9(a)–(c). The results indicated that AxG7F0.4 hydrogels exhibit favorable biocompatibility, while formulations with lower alginate concentrations (A0.5G7F0.4) showed enhanced bioactivity. Meanwhile, C2C12 cells began to fuse, which is the key step for differentiation into muscle fibers, indicating that AxG7F0.4 is suitable for the construction of muscle tissues and biological hybrid robots *in vitro*. To enable a quantitative comparison of the cellular metabolic activity of AxG7F0.4 and MFT hydrogels, ECCK-8 assays were performed.
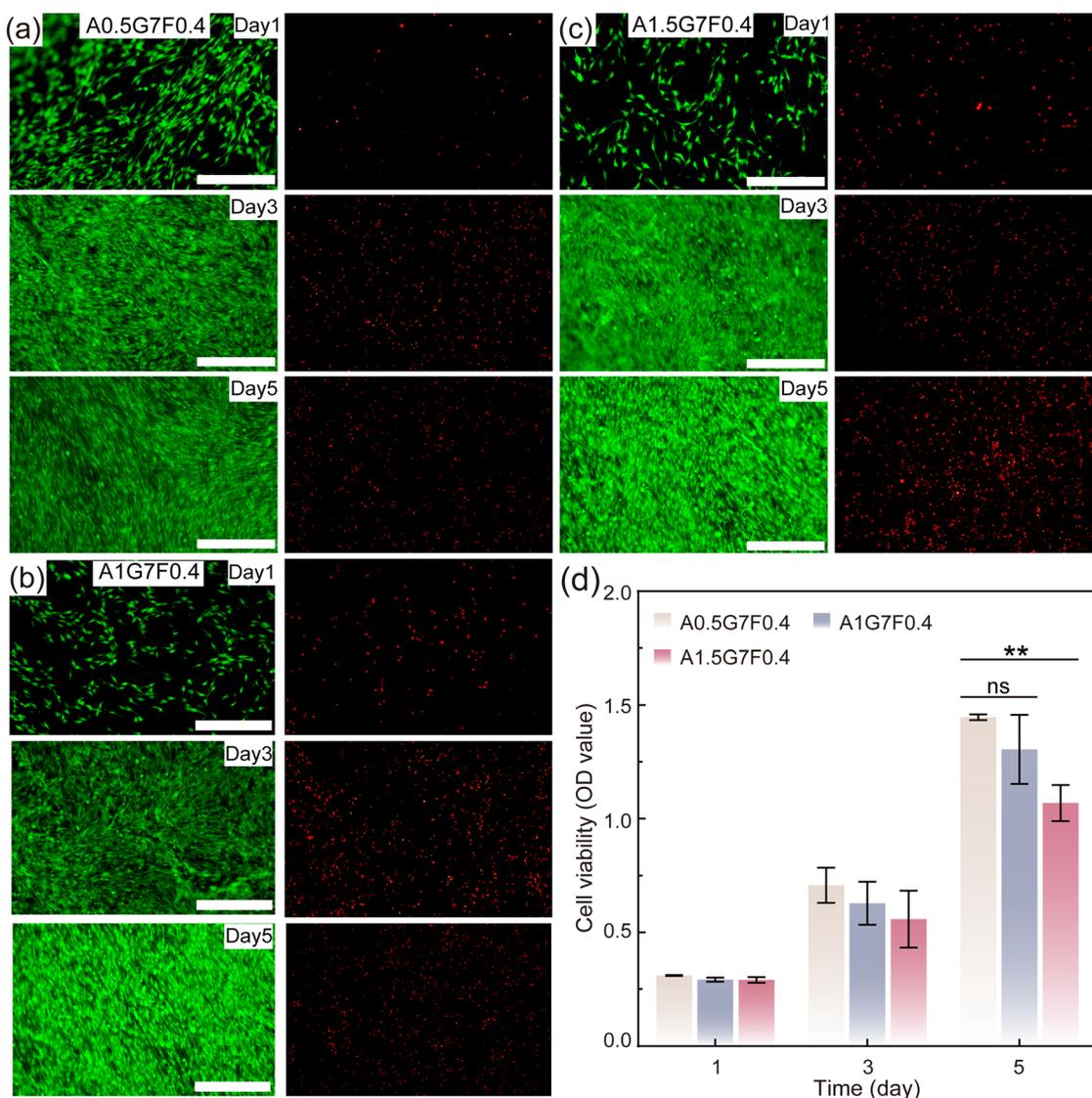

Fig. 9 Cell viability results. Live/dead staining assay of the (a) A0.5G7F0.4, (b) A1G7F0.4 and (c) A1.5G7F0.4 hydrogels. (d) ECCK-8 test results. The scale bar is 400 μm. ***$p < 0.001$, **$p < 0.01$ and *$p < 0.05$.

This journal is © The Royal Society of Chemistry 2025

J. Mater. Chem. B, 2025, **13**, 9824–9837 | **9835**

The ECCK-8 kit was used to quantify cell viability in the hydrogels in 96-well plates seeded with 1500 cells per well. During days 1–3, A0.5G7F0.4 exhibited higher cell viability than A1G7F0.4 and A1.5G7F0.4, while no significant difference was observed. The OD values of A0.5G7F0.4, A1G7F0.4, and A1.5G7F0.4 on day 5 were about 1.45 ± 0.113, 1.30 ± 0.152, and 1.07 ± 0.08, respectively (Fig. 9(d)). Statistical analysis confirmed no significant difference between A0.5G7F0.4 and A1G7F0.4 ($p > 0.05$), whereas A0.5G7F0.4 maintained significantly higher viability *versus* A1.5G7F0.4 ($p < 0.05$). These results indicate that increased alginate concentration adversely affects cell viability, probably because alginate is an inert biomaterial with insufficient mammalian cell adhesion molecules or protein adsorption capacity and hence has limited capability for cell attachment or interactions.[29]

Concurrently, AxG7F0.4 exhibited lower cell viability than that reported previously for MFT hydrogels (4.075 ± 0.115)[9] inoculated with equivalent cell numbers. The reduced cell viability in AxG7F0.4 compared with that in MFT may be due to alginate incorporation, which provides substantially fewer cell-adhesive ligands than the ligand–abundant and intact laminin/collagen IV networks present in the Matrigel. To further improve overall cell viability, the concentration of fibrinogen and gelatin in the composite hydrogel can be increased.

4. Conclusion

In this study, we successfully fabricated alginate–gelatin–fibrinogen hydrogels with high performance stability, excellent printability, low swelling behavior, tunable mechanical properties, and ease of handling. The experimental results demonstrate that the proposed method successfully addresses four existing limitations of MFT hydrogel materials used for bio-hybrid robot fabrication. Meanwhile, the alginate–gelatin–fibrinogen hydrogel can also dynamically regulate the mechanical properties of the material through a triple cross-linking method, broadening its window of desired mechanical properties. The C2C12 cell culture results and printed structures demonstrate that this material is suitable for the 3D-printing-based fabrication of complex muscle tissue architectures and biohybrid robots.

In subsequent works, we will further study the impacts of controlled adjustment of the modulus of *in vitro* constructed tissues at various time points during three-dimensional cell culture to facilitate advanced tissue regeneration efforts and biohybrid robotics. A quantitative analysis of the relationship between printed microfiber geometry and cellular response (*e.g.*, differentiation *vs.* fiber width) will further elucidate design principles for advanced bio-robotic systems, with a parallel evaluation of muscle repair efficacy.

Author contributions

Zening Lin designed the study and wrote the original draft; Yang Hong, Yun Yang, Yuan Gao, and Hang Xie analyzed the data; Tao Jiang and Zirong Luo revised the manuscript and provided the funding.

Conflicts of interest

The authors declare no conflict of interests.

Data availability

Data are available upon request from the authors.

Acknowledgements

References

1 S. Kalidas and S. Sumathi, *J. Mater. Res. Technol.*, 2025, **34**, 1850–1864.

2 D. Trucco, R. Gibney, L. Vannozzi, G. Lisignoli, D. J. Kelly and L. Ricotti, *J. Mater. Res. Technol.*, 2025, **36**, 358–368.

3 S. Y. Lee, H. J. Hwang, Y. J. Song, D. Lee, B. Ku, J. K. Sa and D. W. Lee, *Mater. Today Bio*, 2023, **23**, 100793.

4 E. Ko, Z. Li, L. Gapinske, K.-Y. Huang, T. Saif and H. Kong, *Biomaterials*, 2022, **287**, 121643.

5 M. Askari, M. A. Naniz, M. Kouhi, A. Saberi, A. Zolfagharian and M. Bodaghi, *Biomater. Sci.*, 2021, **9**, 535–573.

6 J. Schöneberg, F. De Lorenzi, B. Theek, A. Blaeser, D. Rommel, A. J. C. Kuehne, F. Kießling and H. Fischer, *Sci. Rep.*, 2018, **8**, 10430.

7 L. Yang, C. Zhang, R. Wang, Y. Zhang, Q. Zhang, H. Qin and L. Liu, *Adv. Funct. Mater.*, 2024, **35**, 2410334.

8 Y. Kim, Y. Yang, X. Zhang, Z. Li, A. Vázquez-Guardado, I. Park, J. Wang, A. I. Efimov, Z. Dou, Y. Wang, J. Park, H. Luan, X. Ni, Y. S. Kim, J. Baek, J. J. Park, Z. Xie, H. Zhao, M. Gazzola, J. A. Rogers and R. Bashir, *Sci. Robotics*, 2023, **8**, eadd1053.

9 Z. Lin, T. Jiang, Y. Yang, Y. Hong, Y. Gao, H. Xie and Z. Luo, *Appl. Mater. Today*, 2024, **39**, 102315.

10 T. Jiang, J. G. Munguia-Lopez, K. Gu, M. M. Bavoux, S. Flores-Torres, J. Kort-Mascort, J. Grant, S. Vijayakumar, A. De Leon-Rodriguez, A. J. Ehrlicher and J. M. Kinsella, *Biofabrication*, 2020, **12**, 015024.

11 R. Landers, U. Hübner, R. Schmelzeisen and R. Mülhaupt, *Biomaterials*, 2002, **23**, 4437–4447.

12 T. Distler, C. Polley, F. Shi, D. Schneidereit, M. Ashton, O. Friedrich, J. Kolb, J. Hardy, R. Detsch, H. Seitz and A. Boccaccini, *Adv. Healthcare Mater.*, 2021, **10**, 2001876.

9836 | *J. Mater. Chem. B*, 2025, **13**, 9824–9837

This journal is © The Royal Society of Chemistry 2025

13 M. D. Giuseppe, N. Law, B. Webb, R. A. Macrae, L. J. Liew, T. B. Sercombe, R. J. Dilley and B. J. Doyle, *J. Mech. Behav. Biomed. Mater.*, 2018, **79**, 150–157.

14 Z. Chen, C. Huang, H. Liu, X. Han, Z. Wang, S. Li, J. Huang and Z. Wang, *Bio-Des. Manuf.*, 2023, **6**, 550–562.

15 X. Guo, D. Zhu and S. Jian, *Polym. Bull.*, 2023, **36**, 514–520.

16 R. Raman, C. Cvetkovic and R. Bashir, *Nat. Protoc.*, 2017, **12**, 519–533.

17 T. Jiang, J. G. Munguia-Lopez, K. Gu, M. M. Bavoux, S. Flores-Torres, J. Kort-Mascort, J. Grant, S. Vijayakumar, A. De Leon-Rodriguez, A. J. Ehrlicher and J. M. Kinsella, *Biofabrication*, 2019, **12**, 015024.

18 H. Eghbali, M. Sadeghi, M. Noroozi and F. Movahedifar, *J. Mech. Behav. Biomed. Mater.*, 2023, **145**, 106044.

19 B. Lu, M. Ye, J. Xia, Z. Zhang, Z. Xiong and T. Zhang, *Adv. Healthcare Mater.*, 2023, **12**, 2300607.

20 L. Wang, Z. Cui, G. Xu, W. Li, G. Bao, Y. Sun and J. Zhang, *J. Biomed. Eng.*, 2016, **33**, 911–915.

21 T. Jiang, Z. Lin, X. Qiao, Y. Yang, Y. Hong, J. Shang, Z. Luo and J. Matthew Kinsella, *Mater. Lett.*, 2023, **344**, 134450.

22 I. N. Sneddon, *Int. J. Eng. Sci.*, 1965, **3**, 47–57.

23 F. Zhang, H. Zhang, S. Wang, M. Gao, K. Du, X. Chen, Y. Lu, Q. Hu, A. Du, S. Du, J. Wang, K. Shi, Z. Chen, Z. Li, Z. Li and J. Xiao, *Nat. Commun.*, 2025, **16**, 3738.

24 T. Jiang, J. G. Munguia-Lopez, S. Flores-Torres, J. Grant, S. Vijayakumar, A. D. Leon-Rodriguez and J. M. Kinsella, *Sci. Rep.*, 2017, **7**, 4575.

25 Z. Lin, T. Jiang, J. M. Kinsella, J. Shang and Z. Luo, *Mater. Lett.*, 2021, **303**, 130480.

26 H. Duong, B. Wu and B. Tawil, *Tissue Eng., Part A*, 2009, **15**, 1865–1876.

27 X. Liu and R. Sun, *J. Mater. Res. Technol.*, 2025, **36**, 913–921.

28 Q.-Q. Wang, Y. Liu, C.-J. Zhang, C. Zhang and P. Zhu, *Mater. Sci. Eng., C*, 2019, **99**, 1469–1476.

29 B. Sayyar, M. Dodd, L. Marquez-Curtis, A. Janowska-Wieczorek and G. Hortelano, *Artif. Cells, Nanomed., Biotechnol.*, 2014, **42**, 102–109.